Title

High-Density, Long-Lasting, and Multi-region Electrophysiological Recordings Using Polymer Electrode Arrays

Journal

Neuron, 101(1)

ISSN

0896-6273

Authors

Chung, Jason E
Joo, Hannah R
Fan, Jiang Lan
et al.

Publication Date

2019

DOI

10.1016/j.neuron.2018.11.002

Peer reviewed

HHS Public Access

Author manuscript

Neuron. Author manuscript; available in PMC 2020 January 02.

Published in final edited form as:

Neuron. 2019 January 02; 101(1): 21–31.e5. doi:10.1016/j.neuron.2018.11.002.

High-density, long-lasting, and multi-region electrophysiological recordings using polymer electrode arrays

Jason E. Chung[1,2,*], **Hannah R. Joo**[1,2], **Jiang Lan Fan**[3], **Daniel F. Liu**[2,3], **Alex H. Barnett**[4], **Supin Chen**[5,6], **Charlotte Geaghan-Breiner**[2], **Mattias P. Karlsson**[7], **Magnus Karlsson**[7], **Kye Y. Lee**[5], **Hexin Liang**[2], **Jeremy F. Magland**[4], **Jeanine A. Pebbles**[5], **Angela C. Tooker**[5], **Leslie F. Greengard**[4,9], **Vanessa M. Tolosa**[5,6], and **Loren M. Frank, Ph.D.**[2,8,10,*] **[Professor]**

[1]Medical Scientist Training Program and Neuroscience Graduate Program, University of California San Francisco, CA 94158, USA.

[2]Kavli Institute for Fundamental Neuroscience, Center for Integrative Neuroscience, and Department of Physiology, University of California San Francisco, CA 94158, USA.

[3]Bioengineering Graduate Program, University of California San Francisco, CA 94158, USA.

[4]Center for Computational Biology, Flatiron Institute, 162 Fifth Avenue, New York, NY 10010, USA.

[5]Center for Micro-and Nano-Technology, Lawrence Livermore National Laboratory, Livermore, CA 94550, USA.

[6]Current address: Neuralink Corp., San Francisco, CA 94107, USA.

[7]SpikeGadgets llc., San Francisco, CA 94158, USA.

[*]**Email addresses of corresponding authors** Jason E. Chung, Jason.Chung@ucsf.edu, Loren M. Frank, loren@phy.ucsf.edu.
Lead contact, Loren M. Frank Ph.D., Professor, Howard Hughes Medical Institute, Kavli Institute for Fundamental Neuroscience, Department of Physiology – Box 0444, Sandler Neuroscience Building Rm 514F, San Francisco, California 94143, Tel: 415-502-7357

Author Contributions

J.E.C. and L.M.F. designed the experiments. J.E.C. developed the surgical methodology. J.E.C., H.R.J., J.F., C.G.B., and H.L. collected rodent datasets. J.E.C. analyzed the rodent data. J.E.C., J.F.M., A.H.B., L.M.F., and L.F.G., developed the drift-tracking spike sorting methodologies. J.E.C., V.M.T., S.C., A.C.T., K.Y.L., and L.M.F. designed the polymer array geometries. V.M.T., S.C., A.C.T., and K.Y.L. developed fabrication methodology and fabricated the polymer probes. J.E.C., M.P.K., M.K., D.F.L., and L.M.F. designed the acquisition hardware. J.E.C. and L.M.F. wrote the manuscript with assistance from all authors.

Declaration of Interests

J.E.C and L.M.F. are inventors on a pending patent related to the work described here. M.P.K. and M.K. are co-founders of SpikeGadgets, the company that built the acquisition hardware.

CONTACT FOR REAGENT AND RESOURCE SHARING

Further information and requests for resources should be directed to and will be fulfilled by the Lead Contact, Loren Frank (loren@phy.ucsf.edu).

DATA AND SOFTWARE AVAILABILITY

Data availability

The data that support the findings of this study will be made available upon reasonable request.

Code availability

Electrode-drift spike sorting code is available at https://github.com/magland/msdrift. This code is designed to be a package added to the core MountainSort software, available at https://github.com/flatironinstitute/mountainsort. The analysis code used in this study will be made available upon reasonable request.

[8]Howard Hughes Medical Institute.

[9]Courant Institute, NYU, New York, NY 10012, USA.

[10]Lead contact

Summary

The brain is a massive neuronal network, organized into anatomically distributed sub-circuits, with functionally relevant activity occurring at timescales ranging from milliseconds to months. Current methods to monitor neural activity, however, lack the necessary conjunction of anatomical spatial coverage, temporal resolution, and long-term stability to measure this distributed activity. Here we introduce a large-scale, multi-site, extracellular recording platform that integrates polymer electrodes with a modular stacking headstage design supporting up to 1024 recording channels in freely behaving rats. This system can support months-long recordings from hundreds of well-isolated units across multiple brain regions. Moreover, these recordings are stable enough to track large numbers of single units for over a week. This platform enables large-scale electrophysiological interrogation of the fast dynamics and long-timescale evolution of anatomically distributed circuits, and thereby provides a new tool for understanding brain activity.

ETOC:

Chung et al. present a large-scale, multi-site, polymer electrode-based recording platform. The modular system is capable of data collection from up to 1024 channels in freely-behaving rats, enabling long-term studies of distributed networks

Introduction

An ideal method to observe brain dynamics would monitor many neurons, have high spatial and temporal resolution, enable access to multiple regions located anywhere in the brain, and be usable in awake, freely behaving subjects. Recent work illustrates the potential power of this approach in producing scientific insight: spiking activity from 100–250 simultaneously recorded units within one region can be used to discover single-event content and dynamics (Pfeiffer and Foster, 2013, 2015), activity structure that is not possible to resolve with fewer recorded neurons. Indeed, in the spatial domain, if it were possible to record from similarly high numbers of neurons from multiple brain regions, analogous discoveries in distributed neural computation and function are likely to follow. Furthermore, in the temporal domain, if it were possible not only to record at millisecond precision, but to do so continuously over the span of hours, days, and weeks, such access could yield transformative insight into neural dynamics. Here, too, previous experimental efforts suggest this possibility: recording small numbers of neurons over the span of days has revealed surprising long-timescale firing patterns with functional implications, particularly with respect to learning (Hengen et al., 2013; Hengen et al., 2016).

Most current approaches are optimized exclusively for either the spatial or temporal domain. For example, one-and two-photon imaging can provide long-lasting, cell-type specific, and stable sampling of neuronal populations, but are limited by the temporal resolution and signal to noise ratio of the indicators (Chen et al., 2013), making it difficult to infer the

precise timing of single spikes *in vivo*. Further, these methods do not permit continuous (24 hours a day, 7 days a week) recordings of brain activity. In contrast, electrophysiological approaches provide excellent temporal resolution, but technologies available in awake, freely-behaving animals are generally limited in their unit yields, spatial coverage, signal longevity, signal stability, and/or adaptability for continuous recording. Current silicon fabrication techniques enable close-packed microelectrodes (Scholvin et al., 2016), thereby allowing for dense samplings from a single device, but in a preconfigured geometry. For example, the recently developed Neuropixels probe (Jun et al., 2017) allows for recordings from 384 of 960 total sites, but the recording sites are collinear, and it remains to be established whether long-term tracking of individual neurons is possible. Conversely, long term, continuous recordings of small numbers of neurons were recently documented with a 64-channel tetrode-based system (Dhawale et al., 2017), but this approach does not provide a clear path to recordings from much larger ensembles.

Here we introduce a polymer probe-based system that overcomes the limitations of currently available technologies. Polymer devices achieve the modularity and longevity of microwires while approaching the recording contact density of current silicon devices. Polymer arrays can also provide a neural interface that is biocompatible (Jeong et al., 2015; Kim et al., 2013; Lee et al., 2017a; Luan et al., 2017) and flexible enough to move with the brain, thereby reducing shearing damage of the array on neural tissue (Gilletti and Muthuswamy, 2006). Until now, however, polymer arrays capable of resolving single neurons had not been developed past proof-of-concept (Kuo et al., 2013; Luan et al., 2017; Rodger et al., 2008; Seo et al., 2015; Seo et al., 2016; Tooker et al., 2014; Xie et al., 2015). Our system makes it possible to measure the activity of hundreds of single neurons across multiple, anatomically distant structures in freely-behaving animals. The system furthermore supports continuous 24/7 recording and yields high quality, large-scale single unit recordings for at least five months. In conjunction with this recording system, we adapt the MountainSort (Chung, Magland, et al. 2017) spike sorting system to link clustered units across time segments, demonstrating stable recordings from 21% of individual neurons for over a week.

Results

Modular implantation platform

Simultaneous, large-scale single-unit recording in a distributed neural circuit requires that recording electrodes be flexibly distributed across the brain, and at high enough density to yield hundreds of putative single neurons. In the past this has necessitated a choice between a few high-density arrays with rigid geometries, or many lower-density arrays (or single channels) that can be arbitrarily and precisely distributed across the brain. Our approach in rats, outlined in Fig. 1A, reduces the need for this tradeoff, allowing for high-resolution sampling across multiple targeted regions.

Multishank polyimide electrode arrays form the modular implantable unit, fabricated using a process described previously (Tooker et al., 2012a, b). Each 32-or 64-channel array utilizes a new design for single-unit recording in rat cortex, consisting of two or four shanks respectively, with 16 channels per shank in a dual-line layout (Fig. 1B). Each recording contact consists of a platinum electrode covered by electrically deposited PEDOT-PSS, as

previously developed (Ludwig et al., 2006). Each 32-channel device has an attached 32-channel Omnetics connector, two of which can be accommodated by the pair of mating connectors on each custom printed circuit board (PCB). The same PCB has a readily-available 64-channel amplifying, digitizing, and multiplexing chip (INTAN technologies) wire-bonded to it. An alternative 64-channel PCB replaced the Omnetics connectors with ENEPIG plated pads where the 64-channel arrays were directly wire bonded to the PCB. The resulting modules (Fig. 1C) can be stacked using mezzanine connectors and connected to a custom field programmable gate array (FPGA, SpikeGadgets LLC) which supports up to two stacks of eight modules, for a total of 1024 channels (Fig. 1D). The stacking modules and FPGA are the core hardware of our novel recording system. The FPGA synchronizes the modules and converts the serial peripheral interface bus (SPI) signal from each module to high-definition multimedia interface (HDMI) format, allowing the use of consumer hardware. The 1024 channel, 30 KHz / channel data is streamed via a micro-HDMI cable through a low-torque HDMI commutator (SpikeGadgets LLC) and data acquisition main control unit (MCU, SpikeGadgets LLC) to the data acquisition computer where it is visualized and saved (Fig. 1E). Streaming high speed data through a HDMI commutator enables robust continuous recordings.

The flexibility of polyimide arrays increases biocompatibility (Lee et al., 2017a) but presents a challenge to implantation. Here we employ a detachable silicon stiffener insertion system based upon our previously developed methodology (Felix et al., 2013). Of note, the silicon stiffeners have a thickness of 30 μm and width of 60 μm, as well as a sharp tip angle of 25°. These features make for a low cross-sectional area and reduce trauma on insertion. Stiffener-attached arrays are inserted serially into brain tissue and subsequently tethered to a custom 3d-printed base piece, which is contoured and anchored to the skull (Supplemental Fig. 1; See Methods for detailed description of the implantation procedure). Serial insertion allows multiple arrays to be placed within a single brain region (<1 mm between inserted probes). The rest of the implant is then assembled intraoperatively; silicone gel is added to stabilize the brain and form a protective layer over the polyimide arrays. Next, silicone elastomer is added to protect the polymer arrays from damage and active electronic components from moisture. The entire system is then protected with a custom 3d-printed casing and passive aluminum heatsinks for impact resistance and heat dissipation (Supplemental Fig. 1).

The result was an implant that drew 1.48 watts (0.435 Amps at 3.4 V) and weighed 81g, including 31g dedicated to heat management, providing 0.0115 m^2 of surface area. During data collection, the temperature of the heat sinks was 41–42° C (measured by IR thermometer, room ambient temperature 21° C), only slightly above rat body temperature. After three weeks of recovery post implantation, the animal's movement was only mildly impeded by the weight and typically ran 400 – 600 meters per day when performing spatial behaviors.

Recordings of hundreds of single units distributed across multiple regions

Information processing in the brain depends on the millisecond-timescale interactions of large populations of single neurons distributed across multiple regions. To demonstrate our platform's ability to resolve network events spanning multiple regions, we examined data

from an animal implanted with the full 16-module system. Of these, 8 modules were used for single-unit recording, 2 modules were used for local field potentials, and the remaining 6 had a device or implantation failure (4 were implanted too superficially, 1 module had an intermittently connected headstage chip, and 1 had low-quality and highly correlated signal of unknown cause, see methods for more details). Data were collected during a rest period in a familiar environment. Spike sorting using MountainSort (Chung, Magland, et al. 2017) on data from these 512 channels 45 days after implantation produced 1533 clusters with a continuum of qualities. The clusters were then stratified using our previously established (Chung, Magland, et al. 2017) *k*-nearest neighbor-based cluster quality metrics, isolation and noise overlap. These per-cluster metrics rely on the proportion of that cluster's events whose nearest neighbor is from the same cluster versus another cluster (isolation) or an empirically generated noise cluster (noise overlap). Three hundred seventy five of the 1533 clusters exceeded our previously established (Chung, Magland, et al. 2017) thresholds (isolation > 0.96, noise overlap < 0.03), and are henceforth considered single units (Fig. 2A). The modules used for single unit recording were distributed among medial prefrontal cortex (mPFC, n = 2 modules), orbitofrontal cortex (OFC, n = 4 modules), and ventral striatum (VS, n = 2 modules), and polymer probes designed for recording local field potentials (LFP) were targeted to the hippocampus (HPC, n = 2 modules) (Fig. 2B).

Coordination across multiple regions during hippocampal sharp wave-ripples

The simultaneous recording of single units across multiple regions makes it possible to examine cross-area coordination. To illustrate the power of this approach for the study of distributed brain events, we focused on times when we detected hippocampal sharp wave-ripples (SWRs). The SWR is an correlate of synchronous hippocampal population firing implicated in memory consolidation, memory retrieval and planning (Buzsaki, 2015), and is known to engage activity across the majority of the brain (Logothetis et al., 2012). These earlier studies (Khodagholy et al., 2017; Logothetis et al., 2012) leveraged methods that had large spatial coverage but were lacking in single-unit resolution. Complementary studies utilizing dual-site recordings revealed that neurons across many cortical (Chrobak and Buzsaki, 1996; Isomura et al., 2006; Jadhav et al., 2016; Ji and Wilson, 2007; Sirota et al., 2003) and subcortical regions (Dragoi et al., 1999; Lansink et al., 2009; Pennartz et al., 2004) show changes in firing rates around the time of SWRs, and that the specific set of active hippocampal neurons during each SWR can predict the set of active cortical neurons, indicating hippocampal-cortical coordination (Jadhav et al., 2016; Rothschild et al., 2017; Yu et al., 2017).

These findings suggest the possibility of brain-wide coordination at the time of SWRs, but whether these events engage coordinated populations across multiple regions outside the hippocampus remains unknown. We therefore examined activity patterns across the mPFC, VS and OFC during SWRs. We found that changes in activity across the population of 375 single units was evident during individual SWRs (Fig. 2C, D). Across all SWRs, these changes result in significant increases and decreases in firing of a subset of units in each region (Fig. 2E). We confirmed previous reports of mPFC and NAc modulation (Lansink et al., 2009; Tang et al., 2017; Wierzynski et al., 2009): 19 of 61 mPFC ($p < 1.0e-4$ as compared to expected proportion, z-test for proportions) and 27 of 118 NAc units ($p <$

1.0e-4, z-test for proportions) showed SWR modulation based on a $p < 0.05$ threshold (see methods). Of the 19 modulated mPFC cells, 13 were positively modulated and 6 were negatively modulated. Of the 27 modulated NAc units, 24 were positively modulated and 3 were negatively modulated. To our knowledge, SWR modulation of OFC activity has not been examined, and we also found that 28 of 196 OFC units were SWR-modulated ($p <$ 1.0e-3 z-test for proportions). Of the 28 modulated OFC units, 18 were positively modulated and 10 were negatively modulated, providing a further confirmation that SWR events engage activity across many cortical and sub-cortical regions.

The large number of simultaneously recorded single units made it possible to show that spiking patterns are coordinated across multiple regions during SWRs. We used cross-validated generalized linear models (Rothschild et al., 2017) to determine whether ensemble firing patterns in mPFC, NAc, or OFC could significantly predict the firing rate of individual cells in the other regions at the times of SWRs (see Methods). This prediction was highly significant for all pairs of regions (prediction gains reported as mean ± standard error and p-values are from two-tailed Wilicoxon rank sum test: mPFC predicting NAc, 1.16 ± 0.01, shuffle 1.00 ± 9.8e-5, p = 1.7e-74; mPFC predicting OFC, 1.09 ± 0.01, shuffle 1.00 ± 9.1e-5, p = 8.2e-116; NAc preding mPFC, 1.23 ± 0.02, shuffle 1.00 ± 7.7e-5, p = 1.5e-38; NAc predicting OFC, 1.10 ± 0.01, shuffle 1.00 ± 1.1e-4, p = 2.1e-109; OFC predicting mPFC, 1.21 ± 0.02, shuffle 1.00 ± 3.2e-4, p = 9.8e-37; OFC predicting NAc, 1.15 ± 0.01, shuffle 1.01 ± 4.5e-4, p = 7.5e-54; Fig. 2E). Together, these findings illustrate the power of large-scale, distributed recordings and provide the first evidence of coordinated firing patterns across multiple regions during SWRs.

Longevity of single-unit recording

While polymer devices have shown promise in achieving a long-term, biocompatible interface with neuronal tissue (Kuo et al., 2013; Luan et al., 2017; Rodger et al., 2008; Tooker et al., 2014; Xie et al., 2015), their benefits have not yet been combined in configurations and systems capable of sampling many neurons simultaneously. To evaluate the high yield single-unit recording capabilities of polymer arrays in the long term, we implanted three rats with polymer probes into mPFC or OFC and collected data for 160 days or more (one 72-ch implant, one 128-ch implant, and one 288-ch implant, see Methods).

These implants yielded long-lasting, high-quality recordings (Fig. 3A), with some initial variability across a six-week timescale, consistent with the brain's recovery from an acute injury and the transition to a stable, chronic response (Supplementary Fig. 2). Subsequently, recording yield was stable until the end of recording (experiments terminated at 160 days to ensure the availability of histology), yielding up to 45 total units on an individual shank and ~1 single-unit per contact on average (Fig. 3A). Importantly, even after 160 days, our system continued to yield well-isolated individual single units (Fig. 3B), showing no sign of being truncated by the detection threshold (Fig. 3C) and having very few refractory period violations (Fig. 3D). In one case we extended our recordings to 283 days and were able to isolate 16 single-units from the dataset collected on this final day, marking an end to a gradual decline in recording yield (from single-units at day 45 post-implant to 16 single-units at 283 days post-implant; Supplemental Fig. 2C).

Stability of recording

The ability to track individual neurons across days depends upon stable recordings and a clustering strategy that is robust to changes in waveform shape resulting from electrode movement relative to neural tissue. We evaluated recording stability following implantation of six 32-channel probes, each with two 16-channel shanks (192 of 288 total implanted channels, see Methods) into each of three animals. We then recorded continuously (with the exception of moving animal between rooms, see Methods) for 10 or 11 days (animal A, day 53 to 63 post-implant, animal B, day 47 to 57 post-implant, animal C, day 42 to 53 post-implant). To challenge our technology and provide a real-world test, animals performed a spatial navigation task three to four times daily, running ~250 meters during each session. Behavioral sessions were performed in two different rooms. Each 16-channel shank yielded ~1.6 Terabytes of data for that period, and these data were divided into 10 segments of 24-hr length and clustered using MountainSort (Chung, Magland, et al. 2017). Subsequently, clusters were linked across segments using a novel simple and conservative mutual nearest-neighbor rule (see Methods and validation in Supplementary Fig. 3A, B).

This approach allowed us to identify 2322 single units from these recordings, each of which could be clustered for at least one 24-hour period. Moreover, we found that we could continuously track a substantial fraction of these units across many days, despite the expected waveform variation (Dhawale et al., 2017). An example of a unit that was tracked for the entire period is shown in Fig. 4A-D, and on this shank, 24 of 41 clusters identified in the first 24-hour segment could be tracked for more than one week of recording (Fig. 4E). Of the 36 implanted shanks, 26 had at least one clustered unit (9 shanks from animal A, 6 animal B, 11 animal C). The remaining shanks had poor signal resulting from either error in targeting with shanks being too superficial (2 shanks animal A, 2 shanks animal B, 1 shank animal C), hardware failures (physical connector breakage in stack disconnecting 4 shanks in animal B), and one case of channels being shorted together (1 shank animal A, otherwise unknown cause).

We quantified long term stability by focusing on the earlier days of the recordings where we had the potential to track single units continuously for 7 or more days. Of the 1150 units clustered on those days, 21% (247 / 1150) could be tracked for 7 days of recording or more (Fig. 4F, Supplemental Fig. 3C, D). This consisted of 247 unique units from the 416 channels of recording (26 shanks with 16 channels each), or 0.59 unique units trackable for 7 days or more per channel, yielding a dataset from these three animals that permits an in-depth analysis of long-timescale changes in single unit activity.

Firing rate stability in a well-learned task

In the absence of external perturbations, the majority of single-neurons show stable responses when measured intermittently across days (Dhawale et al., 2017; Greenberg and Wilson, 2004; McMahon et al., 2014; Rose et al., 2016). Similar observations have been made from daily recordings in rodent mPFC during spatial behaviors from 60 units across 2 days, and 8 units across 6 days (Powell and Redish, 2014), suggesting that rodent mPFC units show stable firing properties in the context of well-learned behaviors. Our goal was therefore to validate our recording and automated drift tracking methods in comparison to

previous findings for rodent mPFC, and to determine whether the observed stability could be confirmed with continuous recordings over longer timescales with a much larger dataset (247 mPFC units followed for a week or more).

We focused on a simple measure of unit activity: mean firing rates. Unsurprisingly, units displayed a large range and diversity of firing rates throughout a day (Hromadka et al., 2008; Mizuseki and Buzsaki, 2013; O'Connor et al., 2010). We chose to focus on times where behavior was similar across days, and therefore chose periods when the subjects were performing a well-learned spatial behavior in a familiar environment. The behavioral states were further subdivided into times when the animal was at low (< 4.0 cm / s) and high (≥ 4.0 cm / s) speeds, as these are known to correspond to different neural states (Kay et al., 2016; Yu et al., 2017). For each unit, firing rates were calculated during these times across all ten (n = 2 rats) or eleven (n = 1 rat) days of continuous recording. Importantly, given the large diversity of firing rates between neurons, observing stable single-unit firing rates could only occur if both single-unit physiologic firing rates were stable and the method correctly identified individual cells across time (note here that our spike sorting methodology does not use rate or timing information).

Our findings both validate our unit tracking and confirm that firing rates taken from similar behavioral epochs show remarkable degrees of stability across many days (see Supplemental Fig. 3E for data from one example animal). We quantified that stability using firing rate similarity (Dhawale et al., 2017) at increasing time lags. We compared the distribution of firing rate similarities of all units that could be tracked for multiple days to the distribution of firing rate similarities for every different cluster pair (i.e. cluster pairs with different cluster ID's), recorded on the same shank, at the same time lag (see Supplemental Fig. 3E for firing rate similarities for data from one animal). These analyses confirmed that units' firing rates were more similar within the same unit than between units across all days of recording for all 3 animals individually (all two-sided Wilcoxon rank sum $p < 1.0e\text{-}15$ low velocity; $p<1.0e\text{-}14$, high velocity), and together (Fig. 4 G, H, all two-sided Wilcoxon rank sum $p < 1.0e\text{-}48$, low velocity; $p < 1.0e\text{-}44$, high velocity).

Putative cell type and tracking length

Finally, as brain networks are made up of interacting populations of excitatory and inhibitory neurons, we asked whether our ability to track units across long timescales extended to both fast-spiking putative interneurons as well as putative excitatory cells. A common approach to differentiating these unit types is via a combination of waveform shape and mean firing rate (Buzsaki, 2004), although the relationship between these features and cell type in the cortex is complex (Bartho et al., 2004). Nonetheless, to ask whether spike and firing rate features interacted with long term tracking, we calculated a mean firing rate and spike width (calculated as peak-to-trough time) for the first hour of data collected in the 26-shank 10-day dataset.

An examination of the relationship between these features revealed a broad distribution of values (Fig. 4 I). We focused on the two extrema of the joint distribution to permit a clear comparison of firing features and tracking, identifying units with firing mean firing rates > 5 Hz and spike widths < 0.5 ms as fast-spiking (FS) and units with firing rates < 3 Hz and

spike widths > 0.5 ms as putative excitory (PE). To eliminate any ambiguity in this classification, we excluded all other units that did not fit either criterion. This resulted in identification of 31 putative interneurons and 268 putative non-interneurons (Fig. 4 I).

We then compared the length of time each putative cell type could be tracked and found that putative interneurons could be tracked for a mean time of 109 hours while putative non-interneurons could be tracked for a mean time of 105 hours (Fig. 4 J), with no statistically significant difference between the two groups (two-sided Wilcoxon rank sum $p = 0.13$). These findings suggest that our system does not have systematic biases in the tracking of units with different waveform and firing rate features.

Discussion

Electrophysiological recordings provide millisecond resolution information about the activity of neurons, and our system makes it possible to access this information simultaneously across hundreds of neurons within a region, in multiple anatomically distant regions, and to do so for a time period spanning months. We demonstrate large-scale recordings from neurons in three widely separated brain structures, the OFC, the mPFC, and the NAc, yielding a conservative total of 375 well-isolated neurons recorded simultaneously. These recordings allowed us to demonstrate widespread and coordinated activation of all three regions at the time of hippocampal SWR events. Moreover, high quality recordings could be obtained across many months. In addition, our system, the first implementation of a high-channel count flexible polymer electrode array-based system, makes it possible to perform continuous 24/7 recording. Together with a novel simple and conservative linking algorithm we tracked 2322 units for 24 hours or more, and 247 (of the 1150 possible, ~21%) of these units across more than a week.

Comparison to existing technologies.

Our system was developed with the explicit goal of enabling large-scale, long-lasting, stable, and spatially distributed recordings across multiple brain regions in freely behaving animals. To make that possible we took advantage of the flexibility and recording stability of polymer electrodes, which had previously been demonstrated in low channel-count implants (Jeong et al., 2015; Kim et al., 2013; Lee et al., 2017a). Extending those low channel-count implants to our modular, 1024 channel system represents a substantial advance, in that we overcame a series of challenges associated with system integration and real-world performance: (1) large rodent implant construction, (2) development of polymer arrays with closely spaced channels to permit accurate spike sorting, (3) insertions of up to 16 polymer devices in the same animal, with up to 3 at < 1 mm spacing, (4) mechanical decoupling of the recording devices from the headstage electronics to permit long term, stable recordings, heat management for 1024 channels being sampled at 30 KHz, and (6) high-bandwidth data acquisition. This propels flexible polymer probe technologies from engineering demonstrations and characterizations of neural damage to application in scientific studies.

This system also provides a set of capabilities complementary to those of recently developed high-density silicon-based arrays (Herbawi et al., 2017; Jun et al., 2017; Lopez et al., 2017; Raducanu et al., 2017; Scholvin et al., 2016). These high-density silicon arrays consist of

both a region with recording contacts that are inserted into neural tissue as well as a region containing active electronics, connectors, and other hardware. The result is a more monolithic device that requires comparatively large volumes close to the brain surface. These devices have also not been shown to be compatible with continuous, 24/7 recording, and the greater rigidity of these devices, as compared to polymer, is likely to impact recording stability. As a result, where our system enables highly distributed, stable, and very long-lasting recordings, silicon devices are particularly well suited for shorter-term recordings in the context of head fixed experiments or experiments where only a small number of devices are used.

Understanding distributed information processing.

Information processing in the brain is distributed, parallel, and dynamic. In contrast, current experiments often focus on a single region, record from small numbers of neurons, and average over many trials to estimate response functions. While these studies provide key insights into brain function, they cannot capture many of the most central elements of neural computation. Our system provides both high density and modularity to allow for recordings of many units across a set of structures of interest, and longevity and stability to study these units across behavioral states and as they evolve. The combination of features of our system – density, modularity, longevity, and stability – enable experimenters to address fundamental, long-standing questions of brain function.

Density and Modularity.

Neural computations depend on local circuits, distributed circuits within a brain region, and widely distributed circuits located across regions. We therefore developed a technology platform designed to sample many neurons across spatial scales. Our individual polymer arrays consist of multiple shanks, each with 16 closely spaced electrode contacts. This geometry allows us to leverage the single unit isolation achievable when multiple electrodes detect signals from the same neurons (Gray et al., 1995) while making it possible to record across multiple insertion sites in the same brain region. These densities resulted in recordings of up to 45 well isolated single units on a shank and on average one unit per recording electrode when devices were placed in neocortex, permitting study of local circuit dynamics in the neighborhood of a shank and, simultaneously, across shanks in the same brain region.

We demonstrated these capabilities with recordings from 375 units distributed across mPFC, OFC and NAc, selected from 1533 identified clusters. The 4-shank, 64-channel probes used here had a larger contact to edge-of-shank distance than the 2-shank, 32-channel probes, which may have contributed to the higher yield per channel seen with the 2-shank versions (Lee et al., 2017b). These recordings allowed us to identify a subset of SWR-modulated OFC neurons and simultaneous modulations of brain activity during hippocampal SWRs across regions. Recordings from populations of this size make it possible to carry out a number of analyses that are either not possible or very difficult with lower unit counts, including simultaneous comparisons of activity patterns across regions. In this respect only the Neuropixels (Jun et al., 2017) probe offers similar recording densities, and in that case the linear arrangement of sites may limit the density of recordings within a single region.

Here we note that while it is tempting to compare recording yields across devices, these comparisons can only be done fairly if the same spike sorting approach is applied in both cases. We used our recently developed, fully automatic spike sorting package MountainSort (Chung, Magland, et al. 2017) and applied conservative cluster quality metrics to ensure that we were only including well isolated units. Nonetheless, these per-channel yields are similar to those reported recently for an acute implantation of two Neuropixels probes, where ~370 units per probe were recorded from the 384 active sites. A direct comparison of the yields of chronically implanted Neuropixels probes is difficult because only one chronically implanted probe's cell yield was reported, which was 127 units 49 days after implantation.

Longevity and Stability.

Experiences drive plasticity in neural circuits, thereby modifying the way they process information. Our system provides the capacity to observe how these changes manifest over the seconds to months during which the network reorganizes. We maintained high quality recordings for 160 days across multiple devices and animals, and extended one set of recordings to 283 days with only a slight decline in recording quality. The consistent high-quality recordings for 160 days reported here also exceed those reported for the latest generations of IMEC devices (Mols et al., 2017), including the immobile, chronically-implanted Neuropixels device, where stable total firing rates and uncurated cluster numbers were reported for recordings spanning 56 days (Jun et al., 2017), although those devices may yield longer recordings than reported.

Finally, we demonstrated stability of recordings that makes it possible to study the same units, 24 hours a day, across at least a week. Using a simple and fully automatic algorithm for matching clustered units across time segments, we first identified 2322 units across three animals that could each be clustered across an at least one 24-hour period. We then focused on the units identified at least seven days before the end of the recording (1150) and found that of those units, we were able to track ~21% (247 / 1150 from 26 shanks) for seven or more days This stability was also achieved in the context of an experiment where animals were running long distances and performing a spatial task across novel and familiar environments.

We note here that our quantification and electrode-drift tracking method provides a conservative estimate of trackable units, and that given the simplicity of our algorithm, it is likely that a more sophisticated approach would allow for even better results. The proportion of units we could track across more than a week is similar to that recently reported for a semi-automatic method applied to data from a 64 channel, 16-tetrode based system, which yielded 19 units per day (Dhawale et al., 2017), less than half of our observed per-channel yield.

Distributed representations and their evolution.

Even relatively simple behaviors, such as the response to a stimulus, are known to engage multiple neural structures. Averaging over multiple trials or stimulus presentations has been a necessity given low simultaneous cell yields, but has nonetheless provided insight into how neural structures can represent information. Single trial dynamics and variability remain

largely understudied due to the required high cell yields. Moreover, less is known about the neural dynamics of single trials across multiple brain structures, requiring high cell yields in multiple structures. Even less is known about how these representations change with time and experience, requiring these same cells and yields to be maintained over time.

This work provides a method for the millisecond-timescale sampling hundreds of cells from multiple anatomically distant regions. This allows detailed single-trial dynamics to be resolved in multiple regions simultaneously. We demonstrated this capability by showing that individual SWRs, known to hold the information of a coherent spatial representation in hippocampus (Pfeiffer and Foster, 2013, 2015), can engage a specific population of neurons across multiple brain structures. Is there any behavioral significance to SWRs that differentially engage specific structures? Do SWRs with the same spatial content drive the same types of responses in other regions? Does this pattern change with learning? Previously inaccessible questions such as these are now within reach.

Moreover, the system is capable of tracking over 20% of single-units for a week or more and thereby enables the measurement of long time scale changes in single-trial dynamics and other neural activity patterns. A number of critical types of information processing, including memory consolidation, are thought to take place on the timescales of hours, days and months, and these data make it possible to further our understanding about how that happens. Data sets made possible by our system can be used to ask many previously unaddressed questions, including how individual unit selectivity changes during experiences and following long periods of sleep, how population activity within an area changes, and even how interactions among distributed brain regions might evolve as information is stored, consolidated and retrieved to inform behavioral choices.

In summary, our system enables the use of large-scale polymer recording arrays in rats, supporting very high channel counts, cell yields, and longevities. This measurement capacity can also be combined with manipulations: polymer recording technologies, like other types of electrodes, are compatible with optogenetic (Seymour et al., 2017; Wu et al., 2013; Zhao et al., 2017) and chemogenetic (Alexander et al., 2009) interventions, and thus this technology opens the door to new types of experiments where large, distributed populations are monitored and manipulated over days, weeks and months. This technology is also suited to translation to other species. In larger animals, where larger impact forces and brain pulsations are present, flexible polymer will likely match or exceed performance of existing chronic recording technologies. The full 22 mm x 22 mm x 25 mm 1024-ch system should fit into existing primate chambers, making its utilization relatively straightforward.

The implantation platform will benefit from future silicon and polymer process advances, which will potentially enable higher channel counts, lower power consumption, and smaller implant sizes. Beyond pure recording applications, the modular design lends itself to integration with new elements that expand the functionality, such as chemical sensing (Tooker et al., 2013; Wassum et al., 2008), optical coupling for circuit manipulations (Li et al., 2018; Rudmann et al., 2018; Wu et al., 2015), and computational power for closed-loop applications.

EXPERIMENTAL MODEL AND SUBJECT DETAILS

Rat

All experiments were conducted in accordance with University of California San Francisco Institutional Animal Care and Use Committee and US National Institutes of Health guidelines. Rat datasets were collected from male Long-Evans rats (RRID: RGD_2308852), 6–23 months of age, with weights ranging from 500–600 g. All rats were fed standard rat chow (LabDiet 5001) in addition to sweetened evaporated milk for reward during behavioral performance. Rats were ordered from Charles River Laboratories at weights of 300–400 g and 3–4 months of age.

METHOD DETAILS

Surgical procedure

Male Long-Evans rats (RRID: RGD_2308852), were implanted with polymer probe(s) at 6–12 months of age. Polymer arrays were targeted to a variety of targets (all coordinates given in millimeters relative to bregma: medial prefrontal cortex (mPFC, including prelimbic and anterior cingulate cortices; ±1.2 ML, +1.5 to +4.5 AP, −2.0 to −4.0 DV, arrays implanted 6–8° transverse from saggital plane, perpendicular to coronal plane), ventral striatum (VS, primarily nucleus accumbens shell; ±0.7 to +1.9 ML, +0.8 to +1.9 AP, −7.2 DV, arrays implanted parallel to midline and perpendicular to coronal), orbitofrontal cortex (OFC, primarily lateral orbitofrontal cortex; ±3.5 to 3.7 ML, +2.6 to +3.4 AP, −4.0 DV, arrays implanted at 54º saggital from coronal plane), dorsal hippocampus (dHPC, ±2.3 to 2.8 ML, −3.5 to −4.0 AP, −4.0 to −6.0 DV, arrays implanted 45º coronal from saggital plane). Also see Supplemental Fig. 1C for view of insertion angles. For some subjects, stimulating electrodes and tetrode microdrives were also implanted at the same time, targeted to the ventral hippocampal commissure (vHC, ±1.0 ML, −1.2 or −2.0 AP) and dHPC.

Anesthesia was induced using ketamine, xylazine, atropine, and isoflurane. Every 4 hours, the animal received additional ketamine, xylazine, and atropine.

The skull was cleaned, targets were marked, and all drilling was completed. Commercially-pure titanium (CpTi) 0–80 set screws (United Titanium, OH), selected for their well-known ability to osseo-integrate (Le Guehennec et al., 2007), were then placed around the perimeter of the implant. Bone dust was cleared from the skull, and craniectomies and durectomies were completed. The skull was briefly allowed to dry and a custom 3d-printed base piece (RGD837 Stratasys, MN) was then fixed to the skull using 4-META/MMA-TBB (Matsumura and Nakabayashi, 1988) (C&B Metabond). This base piece serves a multitude of functions, including acting a reservoir for saline or silicone gel, an anchoring point for the polymer arrays, and a standardized interface from which the rest of the implant can be affixed and constructed during the implantation.

Polymer probes attached to silicon stiffeners by polyethylene glycol (PEG) were then inserted to the brain (Felix et al., 2013). Probe insertion involved several steps prior to the surgery, covered below in the Methods section “preparation of stiffeners and arrays for insertion.” During the surgery, each of the custom 3d-printed insertion pieces (one connected

to the stiffener and polymer array, one to the stiffener only) was attached to two one-axis micromanipulators (MO-10, Narshige). In turn, the insertion device (two 3d-printed pieces and two micromanipulators) was connected to the stereotax. The array was moved to the target and adjusted to avoid surface vasculature and other arrays (1 to 15 minutes). Next, it was quickly (< 5 seconds) lowered ~ 0.5 mm into the brain using the stereotax. A quick initial insertion was required to prevent premature softening of the PEG and detachment of stiffener and array in the cerebrospinal fluid above the brain. Next, a micromanipulator was used to advance the stiffener and the polymer array simultaneously, until reaching the final targeted depth. The stiffener and array were lowered at a rate of ~ 25 μm / second until within 1 mm of the final depth, at which time the rate was reduced to ~ 5 μm / second (3 to 6 minutes).

Once at final depth, the polymer array was affixed to the 3d-printed base piece using light-curable dental acrylic (Vivid Flow, Pearson Dental; 2 to 4 minutes). Next, the 3d-printed base piece was filled with saline and additional saline was dripped onto the silicon stiffener until the PEG dissolved (1 to 2 minutes). The silicon stiffener was retracted using the second micromanipulator at a rate of ~ 5 μm / second for the first 1 mm, and then at a rate of ~ 25 μm / second until the silicon stiffener was above brain surface (3 to 4 minutes). Gentle bends were allowed to form below the anchoring points on the polymer arrays, acting as strain relief. The time from mounting the insertion device to the stereotax to completion of stiffener retraction typically took 10 to 25 minutes, and largely depended on the surface vasculature and nearby arrays. Insertion was repeated for all targeted locations.

After all polymer probes were affixed, the saline filling the 3d-printed base piece was then removed and silicone gel (Dow-Corning 3–4680) was used to fill the 3d-printed base piece, providing a means to seal the durectomies and craniectomies, and also provide added support for the polymer arrays. Additional custom 3d-printed pieces were used to construct a protective case around the polymer devices and active electronic components of the implant. Silicone elastomer (Quik-sil, WPI) was then added to the remainder of the exposed polymer, with special attention to the soft polymer – rigid printed circuit board interface, and 3d-printed casing was affixed to the skull using dental acrylic.

Reagents and data acquisition

Polymer arrays—The polymer arrays were fabricated at the Lawrence Livermore National Laboratory nanofabrication facility as described previously (Tooker et al., 2012a, b). Briefly, devices have three trace metal layers and four polyimide layers with a total device thickness of 14 μm. All arrays had a tip angle of 45°.

Devices with an LFP configuration had 20 μm contacts in a single-line with a center-to-center distance of 100 μm, tapered shank width of 61 μm to 80 μm, 21 or 22 contacts per shank, and an edge-of-shank to edge-of-shank distance of 420 μm (center-of-shank to center-of-shank distance or pitch of 500 μm).

Devices with a 4-shank, 64-channel single-unit configuration are diagrammed in Fig. 1 and had an edge-of-shank to edge-of-shank distance of 250 μm (center-of-shank to center-of-shank distance or pitch of 330 μm). This design was used in the 1024-channel rat implant,

and one module was used in a 352-channel implant (one 4-shank 64-channel module alongside six 2-shank 32-channel arrays, and 24 tetrodes).

Devices with a 2-shank, 32-channel single unit configuration had an identical shank layout to the 4-shank configuration with the notable reduction in edge-of-contact to edge-of-shank distance from 12 μm (4-shank design) to 6 μm (2-shank design). This device design was used for the majority of the data shown, used in the 128-channel implant (data shown in Fig. 3), and all 288-channel implants (six, two-shank, 32-channel polymer arrays and 24 tetrodes).

The device with a 2-shank, 36-channel single-unit configuration (featured in Supplemental Fig. 2) had a similar dual-line, staggered design to the other single-unit configurations with a few notable exceptions. The shank width was 100 μm, edge-of-contact to edge-of-shank distance was 12 μm, and 3 of the 18 contacts were placed closer to the tip of the shank.

PEDOT-PSS application and site impedance—The solution used for PEDOT-PSS application consisted of 0.14% by weight 3,4-ethylenedioxythiophene (EDOT) and 0.08% by weight poly(sodium 4-styrenesulfonate) (PSS) in deionized water. Constant current was applied to microelectrodes for PEDOT-PSS deposition at a current density of 3 mA/cm^2 for 50 seconds.

The typical impedances of the 20 μm circular contacts after PEDOT-PSS deposition was less than 100 kOhm at 1 kHz measured in-vitro in the following manner. Electrochemical impedance (EIS) measurements were made using a potentiostat (Princeton Applied Research, AMETEK Inc.) using vendor-supplied software. All measurements were made in a three-electrode cell using a Pt counter electrode, an Ag/AgCl reference electrode, and phosphate-buffered saline (pH 7.5) as the electrolyte.

Silicon stiffeners—The silicon stiffeners had different dimensions than the polymer arrays that they were coupled to. The stiffeners were 30 μm thick and 60 μm wide and centered relative to the 80 μm wide polymer array shanks. This was done to help prevent overflow of the polyethylene glycol from the bond interface to the top of the polymer array. The array and stiffener were both aligned at their tips, although the stiffener had a sharper tip angle of 25º compared to the polymer array's tip angle of 45°.

Preparation of stiffeners and arrays for insertion—Polymer arrays had a 2 cm long x 1 mm thick strip or tube of polyimide attached perpendicular to the length of the array, 10 – 20 mm above the shank tips using UV curable epoxy (Loctite 3974, Henkel). This strip of polyimide was later used for tethering the probe to the implant.

The silicon stiffener and polymer array were bonded together using PEG. This involved PEG application to the silicon stiffener's reservoir and heating of the stiffener using a hot plate. The PEG wicked down the channel etched into each shank of the stiffener. Next, the stiffener and array were aligned such that the tips were overlapping and the array's shanks were centered relative to the stiffener. The stiffener-probe device was then allowed to cool and the

PEG bonded them together. Next, a drop of PEG was placed on top of the polymer probe and silicon stiffener, 2 to 4 mm above the top of the shanks.

The stiffener was fixed to a custom 3d-printed insertion piece (RGD837 Stratasys, MN) using an ethyl cyanoacrylate-based adhesive (Loctite 1363589, Henkel) and the Omnetics connector or PCB bonded to the polymer array was attached to a second custom 3d-printed insertion piece (RGD837 Stratasys, MN). The two 3d-printed pieces were connected using a screw. Once affixed to the 3d-printed insertion pieces, the stiffener and array were sterilized using ethylene oxide (Anprolene AN74i, Andersen products).

16-module, 1024-channel implant—The 16-modules were distributed equally across both hemispheres. Of the 16 modules implanted, 2 were targeted to dHPC. These two arrays were designed for sampling local field potentials and had an electrode pitch of 100 μm (center-to-center distance of 100 μm) with 20 μm circular contacts. Data from these arrays were not used for spike sorting. Of the remaining 14 modules, 4 were targeted to OFC, 4 were targeted to VS, and 6 were targeted to mPFC. Of the 6 devices targeted to mPFC, 4 were implanted too superficially. There were device failures on 2/4 targeted to VS, with one module having an intermittent connection and one module having highly correlated signal, possibly due to a short at the level of the polymer or the PCB.

160 day periodic recordings—Polymer probes were targeted to mPFC or OFC. In one implant, two two-shank 36-channel arrays were implanted into mPFC and recorded from for 263 days, the termination of the experiment due to animal approaching end of life expectancy. This animal was recorded from using the NSpike data acquisition system (L.M.F. and J. MacArthur, Harvard Instrumentation Design Laboratory) in a 13’’ x 13’’ rest box, and was returned to its home cage. The second implant consisted of four 2-shank 32-channel arrays, all targeted to OFC (128-channel implant). The third animal was implanted with six 2-shank 32-channel polymer arrays targeted to mPFC, alongside two stimulating electrodes targeted to vHC, and 24 tetrodes targeted to dHPC bilaterally, for a total of 288-channels of recording. For the longevity analyses, the second and third animals were also recorded from in a 13’’ x 13’’ rest box, but on some unanalyzed days, recordings were also carried out while the animal ran in a spatial environment.

10-day continuous recording in mPFC—Three animals were implanted with six, two-shank, 32-channel polymer arrays targeted to mPFC, alongside two stimulating electrodes targeted to vHC, and 24 tetrodes targeted to dHPC bilaterally. One of the three animals also had one four-shank, 64-channel polymer array targeted to right OFC. This same animal had a device failure resulting in two functional 32-channel polymer arrays in mPFC and one 64-channel polymer array in OFC. Another animal had a commutator failure on day 4 of recording, causing intermittent data loss, and firing rates from this animal’s day of recording were not used for firing rate analyses. Recordings were carried out while animals were housed in their home cages and in alternating epochs of exposure to a familiar rest box and one of two spatial environments in different rooms. Data was not collected when the animal was being moved between rooms with gaps in recording of 15 to 20 minutes in length, with one instance of a 45-minute gap when the commutator failure was discovered. Animals ran

600 – 1000 meters per day in these spatial environments and provided a challenging experimental setting in which to assess recording stability.

On the first day of continuous recording, animals stayed in one room, room A, where they had been performing the same spatial task for several weeks, and performed three behavioral sessions, each lasting 30 −40 minutes. On the second day of recording, animals performed two 30 −40-minute behavioral sessions in room B, their first time being exposed to that room, and then one in room A. On days three through eleven, animals performed two or three sessions of behavior in room B followed by one in room A. Recording was stopped half an hour after the animal finished the session of behavior in room A on day eleven (animals A and B), or day twelve (animal C). In animal C, a twelfth day of recording was carried out with all behavioral sessions occurring in room A. Animals had red/green tracking LED arrays attached to the implant, allowing their position to be extracted from video recorded by a camera mounted to the ceiling.

Histology—Subjects were euthanized with pentobarbital and intracardially perfused with PBS followed by 4% paraformaldehyde in PBS. The brain was post-fixed *in situ* overnight, after which the brain was removed, cryo-protected (30% sucrose in PBS), and embedded in OCT compound. Coronal sections (50 μm) were taken with a cryostat. Sections were stained with NeuroTrace 435/455 Blue Fluorescent Nissl Stain (1:200; Invitrogen, N21479, lot 1846588). Sections were blocked (5% donkey serum in 0.3% Triton-X in PBS, used for all incubations) for 1 hour, incubated with Monoclonal Anti-Glial Fibrillary Acidic Protein (RRID: AB_477010, GFAP, 1:800, Sigma-Aldrich, G-3893, mouse, clone G-A-5, lot 31K4885) overnight, washed, and subsequently incubated with fluorescent secondary antibody (RRID: AB_2736941, Alexa Fluor 488, 1:400, Thermo Fisher Scientific, Z25002).

QUANTIFICATION AND STATISTICAL ANALYSIS

Data processing and analysis

Data analysis was performed using custom software written in Python 3.6.3 (RRID: SCR_008394, Anaconda linux-64 v7.2.0 distribution, Anaconda Inc.) and Matlab 2015b (RRID: SCR_001622, Mathworks).

Spike sorting—Clustering was done using MountainSort, using settings and thresholds as reported previously (Chung, Magland, et al. 2017). Adjacency radius was set to 100 μm when sorting the μm contact, 20 μm edge-to-edge dual-line designs, resulting in clustering neighborhoods of 5 to 9 electrodes. The event detection threshold was set to 3 SD. Putative single-units were identified using previously set thresholds (isolation > 0.96, noise overlap < 0.03) and an automatic merging procedure, reported previously (Chung, Magland, et al. 2017), was used to identify pairs of clusters that corresponded to the higher and lower amplitude components of single units that fired in bursts with decrementing spike amplitudes.

The first step in processing the 240-hr continuous recording datasets was filtering and spatial whitening the entire 240-hr timeseries. Following this, events were detected and clustered in 24-hour segments. Automated curation and bursting-related merging was first completed

independently for each segment. As a result, all clusters in all segments satisfied our criteria for well isolated units. Linking clusters between segments was done using a mutual nearest neighbor rule. For every cluster in the first segment, a 1.66 ms spatially-whitened waveform template was calculated from the last 100 events, using every channel on the shank. Similarly, for every cluster in the second segment, a waveform template was calculated from the first 100 events. Next, the L^2 distance was calculated between every segment 1 and segment 2 pair of templates. If cluster A from segment 1 and cluster A' from segment 2 were mutual nearest neighbors, then the segments were linked.

This approach is conservative as a result of three main features. First, it used only well isolated clusters from each segment, and only matched these well isolated clusters. Second, because the 24-hour segments were not aligned to specific events in the animals' experience, the segments partitioned the spiking activity at points where large, sudden changes in spike amplitudes were very unlikely. Third, the distance calculation was based on whitened spike waveforms from the entire 16 electrode array, yielding unique templates for each unit. The mutual nearest neighbor calculation ensured that these templates matched across the segment boundaries, and we found that this linking algorithm yielded plots of spike amplitude over time that were continuous across the period where the unit could be tracked.

SWR detection and modulation—SWRs were detected as previously described (Cheng and Frank, 2008). Briefly, LFPs from a contact near CA1 was filtered into the ripple band (150 – 250 Hz) and the envelope of band-passed LFPs was determined by Hilbert transform. SWR were initially detected when the envelope exceeded a threshold (mean + 3 SD) on the contact. SWR events were defined as times around the initially detected events during which the envelope exceeded the mean. For SWR-trigged firing rates, only SWRs separated by at least 500 ms were included.

SWR modulation analysis was carried out as described previously (Jadhav et al., 2016). Briefly, spikes were aligned to SWR onset resulting in SWR-aligned rasters. Cells with less than 50 spikes in the SWR-aligned rasters were excluded from these analyses. To determine the significance of SWR modulation, we created 1,000 shuffled rasters by circularly shifting spikes with a random jitter around each SWR and defined a baseline response as the mean of all shuffled responses. We then calculated the mean squared difference between the response in a 0–200 ms window after SWR onset (SWR response) to the baseline. We compared the real SWR response to the 1,000 shuffled responses. We considered a cell as SWR-modulated when the mean squared difference of the SWR response from the baseline was greater than 95% of the shuffled PSTHs. SWR-modulated neurons were further categorized as SWR-excited or SWR-inhibited by comparing the rate in a 0–200 ms window after SWR onset, with the rate of the mean shuffled response in the same 0–200 ms window.

Generalized linear models during SWRs—Construction of generalized linear models (GLMs) was done as reported previously (Rothschild et al., 2017). Briefly, the GLMs were constructed with a log link function to predict spike counts of single units during SWRs in PFC, NAC, or OFC from ensemble spiking patterns in another region. The region's SWR ensemble pattern was the vector of binned spiking responses across units recorded in that region during the 0–200 ms window after SWR onset.

The ensemble patterns were used to predict single cell SWR responses. A single prediction model was generated using predictor data of the ensemble patterns across SWRs, and predicted data of the single-cell SWR responses across SWRs. Only cells that were active (> 0 spikes) in more than 10 SWRs were predicted. For each predictor ensemble and predicted cell, we performed five-fold cross validation. We randomly partitioned the SWRs into five equally sized sets, with the constraint that the number of nonzero values in the predicted vector must be approximately balanced across sets. For each fold, four of five folds was used to train the GLM, and the remaining fold to test. For the test phase, the model derived from the training phase was applied to the predictor ensemble data in the test set, yielding predictions for the predicted cell firing across SWRs.

Prediction error was defined as the mean absolute difference between the predicted spike counts and the real spike counts. For that same fold, we defined a baseline prediction error by performing 100 random shuffles of the predicted firing rates across SWRs in the test fold and taking the mean of the shuffled prediction errors. The real and shuffled prediction errors were then averaged across the five folds. Prediction gain for one predictor-ensemble-predicted-cell combination in one time window was defined as the shuffled prediction error divided by the real prediction error.

For comparison, we repeated the exact same procedure described above on 100 random shuffles of the entire original dataset, where shuffling entailed random matching of activity patterns in the predictor and predicted data (*e.g.*, taking predictor data from one SWR and using it to predict firing rate for another SWR). To assess prediction significance for a pair of regions, we compared the distribution of real prediction gains to the shuffled prediction gains across all ensemble/cell combinations using a two-tailed nonparametric Wilcoxon rank sum test.

Cluster linkage analysis—Quantification of the relative distances of successfully linked cluster pairs to the other possible linked clusters (Supplemental Fig. 3A) was done as follows: if there was a successful link made between cluster A from segment 1 and cluster A’ from segment 2 (A to A’), then the L^2 distances between cluster waveform templates (A and B’), (A and C’), … (B and A’), (C and A’), etc., were normalized to the L^2 distance of (A to A’). These distances, for all successfully linked pairs across all electrode arrays, contributed to the histogram in Supplemental Fig. 3A.

To quantify the distances of successfully linked cluster pairs and their distance to other possible linked clusters relative to the variability of the events within the successfully linked cluster, we normalized the same set of distances as above using the mean spike distance to its template. Specifically, if there was a successful link made between cluster A from segment 1 and cluster A’ from segment 2 (A to A’), the mean of the L^2 distances between the 100 events and the template of A (calculated from the same 100 events) was used as the normalization factor for the L^2 distance from (A to A’), and all other unlinked pairs, (A and B’), (A and C’), … (B and A’), (C and A’), etc. This mean of the L^2 distances is referred to in the text as “event distance.”

In Supplemental Fig. 3B, the normalized distances of successful linkages, (A to A'), contributed to the histogram in red, while the normalized distances of all other unlinked pairs, (A and B'), (A and C'), … (B and A'), (C and A'), etc., contributed to the histogram in black.

Firing rate similarity during behavioral performance—Firing rates were calculated for when the animal was performing the spatial behavior in room A. This constituted ~90 minutes of time on day one (and day twelve in animal C), or ~30 minutes of time on days two through eleven. Roughly half of the time during behavioral performance was spent either at low (< 4.0 cm / s) or high (≥ 4.0 cm / s) velocities.

Firing rate similarity was calculated using the same formula as in (Dhawale et al., 2017), where the similarity of two different firing rates, and was measured by the following formula:

$$FRsimilarity_{i,j} = 1 - 2\left(\frac{abs\left(FR_i - FR_j\right)}{FR_i + FR_j}\right)$$

A firing rate similarity score of 1 occurs when and are identical, and a firing rate similarity score of −1 occurs when one firing rate is 0 (maximally dissimilar). As in (Dhawale et al., 2017), when comparing firing rates for the same unit across time, firing rate similarity was calculated for time lags ranging from 1 to 10 days (animals A and B), or 11 days (animal C, Supplemental Fig. 3). In other words, if a cell could be tracked for all 12 days of behavioral performance in room A, its 1-day time lag firing rate similarity was calculated 11 times (days 1–2, 2–3, …10–11, 11–12), or its 10-day time lag was calculated twice (days 1–11, 2–12).

The distribution of within-unit time lagged similarities was compared to the distribution of all between-unit time lagged similarities, matched for both shank and time lag. This differs from the comparison done in (Dhawale et al., 2017), where time-lagged similarities were compared to the within-day across-unit distribution of firing rate similarities.

KEY RESOURCES TABLE

REAGENT or RESOURCE	SOURCE	IDENTIFIER
Antibodies		
NeuroTrace 435/455 Blue Fluorescent Nissl Stain	Invitrogen	N21479, lot 1846588
Monoclonal Anti-Glial Fibrillary Acidic Protein	Sigma-Aldrich	RRID: AB_477010, G-3893, mouse, clone G-A-5, lot 31K4885
Alexa Fluor 488	Thermo Fisher Scientific	RRID: AB_2736941, Z25002
Experimenta Models: Organisms/Strains		
Male Long-Evans rats	Charles River	RGD_2308852
Software and Algorithms		

REAGENT or RESOURCE	SOURCE	IDENTIFIER
Electrode-drift spike sorting code add-on for MountainSo rt spike sorting software	https://github.com/magland/rnsdrift	commit 5b59a30b5c6b317411870b41d7cb 889db516f67a
MountainSo rt spike sorting software	https://github.com/flatironinstitute/mountainsort	commit 22b7cellf587eb925e7a9f7229fda If6d0690510

Supplementary Material

Refer to Web version on PubMed Central for supplementary material.

Acknowledgments

We thank M. Stryker, K. Ganguly, M. Brainard, and K. Kay for insightful comments, V. Kharzia and A. Kisel for assistance with histology, and M. Borius for assistance with data acquisition hardware. This work was supported by NINDS grant U01NS090537 to L.M.F and V.M.T. and NIMH grant F30MH109292 to J.E.C. The Flatiron Institute is a division of the Simons Foundation.

References

Alexander GM, Rogan SC, Abbas AI, Armbruster BN, Pei Y, Allen JA, Nonneman RJ, Hartmann J, Moy SS, Nicolelis MA, et al. (2009). Remote control of neuronal activity in transgenic mice expressing evolved G protein-coupled receptors. Neuron 63, 27–39. [PubMed: 19607790]

Bartho P, Hirase H, Monconduit L, Zugaro M, Harris KD, and Buzsaki G (2004). Characterization of neocortical principal cells and interneurons by network interactions and extracellular features. J Neurophysiol 92, 600–608. [PubMed: 15056678]

Buzsaki G (2004). Large-scale recording of neuronal ensembles. NatNeurosci 7, 446–451.

Buzsaki G (2015). Hippocampal sharp wave-ripple: A cognitive biomarker for episodic memory and planning. Hippocampus 25, 1073–1188. [PubMed: 26135716]

Chen TW, Wardill TJ, Sun Y, Pulver SR, Renninger SL, Baohan A, Schreiter ER, Kerr RA, Orger MB, Jayaraman V, et al. (2013). Ultrasensitive fluorescent proteins for imaging neuronal activity. Nature 499, 295–300. [PubMed: 23868258]

Cheng S, and Frank LM (2008). New experiences enhance coordinated neural activity in the hippocampus. Neuron 57, 303–313. [PubMed: 18215626]

Chrobak JJ, and Buzsaki G (1996). High-frequency oscillations in the output networks of the hippocampal-entorhinal axis of the freely behaving rat. J Neurosci 16, 3056–3066. [PubMed: 8622135]

Chung JE, Magland JF, Barnett AH, Tolosa VM, Tooker AC, Lee KY, Shah KG, Felix SH, Frank LM, and Greengard LF (2017). A Fully Automated Approach to Spike Sorting. Neuron 95, 1381–1394 e1386. [PubMed: 28910621]

Dhawale AK, Poddar R, Wolff SB, Normand VA, Kopelowitz E, and Olveczky BP (2017). Automated long-term recording and analysis of neural activity in behaving animals. eLife 6.

Dragoi G, Carpi D, Recce M, Csicsvari J, and Buzsaki G (1999). Interactions between hippocampus and medial septum during sharp waves and theta oscillation in the behaving rat. J Neurosci 19, 6191−−6199. [PubMed: 10407055]

Felix SH, Shah KG, Tolosa VM, Sheth HJ, Tooker AC, Delima TL, Jadhav SP, Frank LM, and Pannu SS (2013). Insertion of flexible neural probes using rigid stiffeners attached with biodissolvable adhesive. J Vis Exp, e50609.

Gilletti A, and Muthuswamy J (2006). Brain micromotion around implants in the rodent somatosensory cortex. J Neural Eng 3, 189–195. [PubMed: 16921202]

Gray CM, Maldonado PE, Wilson M, and McNaughton B (1995). Tetrodes markedly improve the reliability and yield of multiple single-unit isolation from multi-unit recordings in cat striate cortex. J Neurosci Methods 63, 43–54. [PubMed: 8788047]

Greenberg PA, and Wilson FA (2004). Functional stability of dorsolateral prefrontal neurons. J Neurophysiol 92, 1042–1055. [PubMed: 15084637]

Hengen KB, Lambo ME, Van Hooser SD, Katz DB, and Turrigiano GG (2013). Firing rate homeostasis in visual cortex of freely behaving rodents. Neuron 80, 335–342. [PubMed: 24139038]

Hengen KB, Torrado Pacheco A, McGregor JN, Van Hooser SD, and Turrigiano GG (2016). Neuronal Firing Rate Homeostasis Is Inhibited by Sleep and Promoted by Wake. Cell 165, 180–191. [PubMed: 26997481]

Herbawi AS, Kiessner L, Paul O, and Ruther P (2017). High-Density Cmos Neural Probe Implementing a Hierarchical Addressing Scheme for 1600 Recording Sites and 32 Output Channels. 2017 19th International Conference on Solid-State Sensors, Actuators and Microsystems (Transducers), 20–23.

Hromadka T, Deweese MR, and Zador AM (2008). Sparse representation of sounds in the unanesthetized auditory cortex. PLoS Biol 6, e16. [PubMed: 18232737]

Isomura Y, Sirota A, Ozen S, Montgomery S, Mizuseki K, Henze DA, and Buzsaki G (2006). Integration and segregation of activity in entorhinal-hippocampal subregions by neocortical slow oscillations. Neuron 52, 871–882. [PubMed: 17145507]

Jadhav SP, Rothschild G, Roumis DK, and Frank LM (2016). Coordinated Excitation and Inhibition of Prefrontal Ensembles during Awake Hippocampal Sharp-Wave Ripple Events. Neuron 90, 113–127. [PubMed: 26971950]

Jeong JW, Shin G, Park SI, Yu KJ, Xu L, and Rogers JA (2015). Soft materials in neuroengineering for hard problems in neuroscience. Neuron 86, 175–186. [PubMed: 25856493]

Ji D, and Wilson MA (2007). Coordinated memory replay in the visual cortex and hippocampus during sleep. Nat Neurosci 10, 100–107. [PubMed: 17173043]

Jun JJ, Steinmetz NA, Siegle JH, Denman DJ, Bauza M, Barbarits B, Lee AK, Anastassiou CA, Andrei A, Aydin C, et al. (2017). Fully integrated silicon probes for high-density recording of neural activity. Nature 551, 232–236. [PubMed: 29120427]

Kay K, Sosa M, Chung JE, Karlsson MP, Larkin MC, and Frank LM (2016). A hippocampal network for spatial coding during immobility and sleep. Nature 531, 185–190. [PubMed: 26934224]

Khodagholy D, Gelinas JN, and Buzsaki G (2017). Learning-enhanced coupling between ripple oscillations in association cortices and hippocampus. Science 358, 369–372. [PubMed: 29051381]

Kim TI, McCall JG, Jung YH, Huang X, Siuda ER, Li Y, Song J, Song YM, Pao HA, Kim RH, et al. (2013). Injectable, cellular-scale optoelectronics with applications for wireless optogenetics. Science 340, 211–216. [PubMed: 23580530]

Kuo JT, Kim BJ, Hara SA, Lee CD, Gutierrez CA, Hoang TQ, and Meng E (2013). Novel flexible Parylene neural probe with 3D sheath structure for enhancing tissue integration. Lab Chip 13, 554–561. [PubMed: 23160191]

Lansink CS, Goltstein PM, Lankelma JV, McNaughton BL, and Pennartz CM (2009). Hippocampus leads ventral striatum in replay of place-reward information. PLoS Biol 7, e1000173. [PubMed: 19688032]

Le Guehennec L, Soueidan A, Layrolle P, and Amouriq Y (2007). Surface treatments of titanium dental implants for rapid osseointegration. Dent Mater 23, 844–854. [PubMed: 16904738]

Lee HC, Ejserholm F, Gaire J, Currlin S, Schouenborg J, Wallman L, Bengtsson M, Park K, and Otto KJ (2017a). Histological evaluation of flexible neural implants; flexibility limit for reducing the tissue response? J Neural Eng 14, 036026. [PubMed: 28470152]

Lee HC, Gaire J, Roysam B, and Otto KJ (2017b). Placing Sites on the Edge of Planar Silicon Microelectrodes Enhances Chronic Recording Functionality. IEEE Trans Biomed Eng

Li BZ, Lee K, Masmanidis SC, and Li M (2018). A nanofabricated optoelectronic probe for manipulating and recording neural dynamics. J Neural Eng 15.

Logothetis NK, Eschenko O, Murayama Y, Augath M, Steudel T, Evrard HC, Besserve M, and Oeltermann A (2012). Hippocampal-cortical interaction during periods of subcortical silence. Nature 491, 547–553. [PubMed: 23172213]

Lopez CM, Putzeys J, Raducanu BC, Ballini M, Wang SW, Andrei A, Rochus V, Vandebriel R, Severi S, Van Hoof C , et al. (2017). A Neural Probe With Up to 966 Electrodes and Up to 384 Configurable Channels in 0.13 mu m SOI CMOS. Ieee T Biomed Circ S 11, 510–522.

Luan L, Wei XL, Zhao ZT, Siegel JJ, Potnis O, Tuppen CA, Lin SQ, Kazmi S, Fowler RA, Holloway S, et al. (2017). Ultraflexible nanoelectronic probes form reliable, glial scar-free neural integration. Sci Adv 3.

Ludwig KA, Uram JD, Yang J, Martin DC, and Kipke DR (2006). Chronic neural recordings using silicon microelectrode arrays electrochemically deposited with a poly(3,4-ethylenedioxythiophene) (PEDOT) film. J Neural Eng 3, 59–70. [PubMed: 16510943]

Matsumura H, and Nakabayashi N (1988). Adhesive 4-META/MMA-TBB opaque resin with poly(methyl methacrylate)-coated titanium dioxide. J Dent Res 67, 29–32. [PubMed: 11039040]

McMahon DB, Jones AP, Bondar IV, and Leopold DA (2014). Face-selective neurons maintain consistent visual responses across months. Proc Natl Acad Sci U S A 111, 8251–8256. [PubMed: 24799679]

Mizuseki K, and Buzsaki G (2013). Preconfigured, skewed distribution of firing rates in the hippocampus and entorhinal cortex. Cell reports 4, 1010–1021. [PubMed: 23994479]

Mols K, Musa S, Nuttin B, Lagae L, and Bonin V (2017). In vivo characterization of the electrophysiological and astrocytic responses to a silicon neuroprobe implanted in the mouse neocortex. Scientific reports 7, 15642. [PubMed: 29142267]

O'Connor DH, Peron SP, Huber D, and Svoboda K (2010). Neural activity in barrel cortex underlying vibrissa-based object localization in mice. Neuron 67, 1048–1061. [PubMed: 20869600]

Pennartz CM, Lee E, Verheul J, Lipa P, Barnes CA, and McNaughton BL (2004). The ventral striatum in off -line processing: ensemble reactivation during sleep and modulation by hippocampal ripples. J Neurosci 24, 6446−−6456. [PubMed: 15269254]

Pfeiffer BE, and Foster DJ (2013). Hippocampal place-cell sequences depict future paths to remembered goals. Nature 497, 74–79. [PubMed: 23594744]

Pfeiffer BE, and Foster DJ (2015). Autoassociative dynamics in the generation of sequences of hippocampal place cells. Science 349, 180–183. [PubMed: 26160946]

Powell NJ, and Redish AD (2014). Complex neural codes in rat prelimbic cortex are stable across days on a spatial decision task. Frontiers in behavioral neuroscience 8, 120. [PubMed: 24795579]

Raducanu BC, Yazicioglu RF, Lopez CM, Ballini M, Putzeys J, Wang SW, Andrei A, Rochus V, Welkenhuysen M, van Helleputte N, et al. (2017). Time Multiplexed Active Neural Probe with 1356 Parallel Recording Sites. Sensors-Basel 17.

Rodger DC, Fong AJ, Wen L, Ameri H, Ahuja AK, Gutierrez C, Lavrov I, Hui Z, Menon PR, Meng E , et al. (2008). Flexible parylene-based multielectrode array technology for high-density neural stimulation and recording. Sensor Actuat B-Chem 132, 449–460.

Rose T, Jaepel J, Hubener M, and Bonhoeffer T (2016). Cell-specific restoration of stimulus preference after monocular deprivation in the visual cortex. Science 352, 1319–1322. [PubMed: 27284193]

Rothschild G, Eban E, and Frank LM (2017). A cortical-hippocampal-cortical loop of information processing during memory consolidation. Nat Neurosci 20, 251–259. [PubMed: 27941790]

Rudmann L, Alt MT, Vajari DA, and Stieglitz T (2018). Integrated optoelectronic microprobes. Current Opinion in Neurobiology 50, 72–82. [PubMed: 29414738]

Scholvin J, Kinney JP, Bernstein JG, Moore-Kochlacs C, Kopell N, Fonstad CG, and Boyden ES (2016). Close-Packed Silicon Microelectrodes for Scalable Spatially Oversampled Neural Recording. Ieee T Bio-Med Eng 63, 120–130.

Seo D, Carmena JM, Rabaey JM, Maharbiz MM, and Alon E (2015). Model validation of untethered, ultrasonic neural dust motes for cortical recording. J Neurosci Methods 244, 114–122. [PubMed: 25109901]

Seo D, Neely RM, Shen K, Singhal U, Alon E, Rabaey JM, Carmena JM, and Maharbiz MM (2016). Wireless Recording in the Peripheral Nervous System with Ultrasonic Neural Dust. Neuron 91, 529–539. [PubMed: 27497221]

Seymour JP, Wu F, Wise KD, and Yoon E (2017). State-of-the-art MEMS and microsystem tools for brain research. Microsystems &Amp; Nanoengineering 3, 16066.

Sirota A, Csicsvari J, Buhl D, and Buzsaki G (2003). Communication between neocortex and hippocampus during sleep in rodents. Proc Natl Acad Sci USA 100, 2065−−2069. [PubMed: 12576550]

Tang W, Shin JD, Frank LM, and Jadhav SP (2017). Hippocampal -Prefrontal Reactivation during Learning Is Stronger in Awake Compared with Sleep States. J Neurosci 37, 11789–11805. [PubMed: 29089440]

Tooker A, Liu D, Anderson EB, Felix S, Shah KG, Lee KY, Chung JE, Pannu S, Frank L, and Tolosa V (2014). Towards a large-scale recording system: demonstration of polymer-based penetrating array for chronic neural recording. Conf Proc IEEE Eng Med Biol Soc 2014, 6830–6833. [PubMed: 25571565]

Tooker A, Madsen TE, Yorita A, Crowell A, Shah KG, Felix S, Mayberg HS, Pannu S, Rainnie DG, and Tolosa V (2013). Microfabricated Polymer-Based Neural Interface for Electrical Stimulation/ Recording, Drug Delivery, and Chemical Sensing -Development. Ieee Eng Med Bio, 5159–5162.

Tooker A, Tolosa V, Shah KG, Sheth H, Felix S, Delima T, and Pannu S (2012a). Optimization of multi-layer metal neural probe design. Conf Proc IEEE Eng Med Biol Soc 2012, 5995–5998. [PubMed: 23367295]

Tooker A, Tolosa V, Shah KG, Sheth H, Felix S, Delima T, and Pannu S (2012b). Polymer neural interface with dual-sided electrodes for neural stimulation and recording. Conf Proc IEEE Eng Med Biol Soc 2012, 5999–6002. [PubMed: 23367296]

Wassum KM, Tolosa VM, Wang J, Walker E, Monbouquette HG, and Maidment NT (2008). Silicon Wafer-Based Platinum Microelectrode Array Biosensor for Near Real-Time Measurement of Glutamate in Vivo. Sensors (Basel) 8, 5023–5036. [PubMed: 19543440]

Wierzynski CM, Lubenov EV, Gu M, and Siapas AG (2009). State-dependent spike-timing relationships between hippocampal and prefrontal circuits during sleep. Neuron 61, 587–596. [PubMed: 19249278]

Wu F, Stark E, Im M, Cho IJ, Yoon ES, Buzsaki G, Wise KD, and Yoon E (2013). An implantable neural probe with monolithically integrated dielectric waveguide and recording electrodes for optogenetics applications. J Neural Eng 10, 056012. [PubMed: 23985803]

Wu F, Stark E, Ku PC, Wise KD, Buzsaki G, and Yoon E (2015). Monolithically Integrated muLEDs on Silicon Neural Probes for High-Resolution Optogenetic Studies in Behaving Animals. Neuron 88, 1136–1148. [PubMed: 26627311]

Xie C, Liu J, Dai X, Zhou W, and Lieber CM (2015). Three-dimensional macroporous nanoelectronic networks as minimally invasive brain probes. Nature Materials 14, 1286–1292. [PubMed: 26436341]

Yu JY, Kay K, Liu DF, Grossrubatscher I, Loback A, Sosa M, Chung JE, Karlsson MP, Larkin MC, and Frank LM (2017). Distinct hippocampal-cortical memory representations for experiences associated with movement versus immobility. eLife 6.

Zhao Z, Luan L, Wei X, Zhu H, Li X, Lin S, Siegel JJ, Chitwood RA, and Xie C (2017). Nanoelectronic Coating Enabled Versatile Multifunctional Neural Probes. Nano letters 17, 4588–4595. [PubMed: 28682082]

Highlights:

- Modular polymer electrode-based system capable of recording up to 1024 channels
- Recording from 375 single units across multiple regions in freely-behaving rats
- Single-unit recording longevity for 160 days post-implantation or more
- System capable of tracking populations of single units continuously for over a week

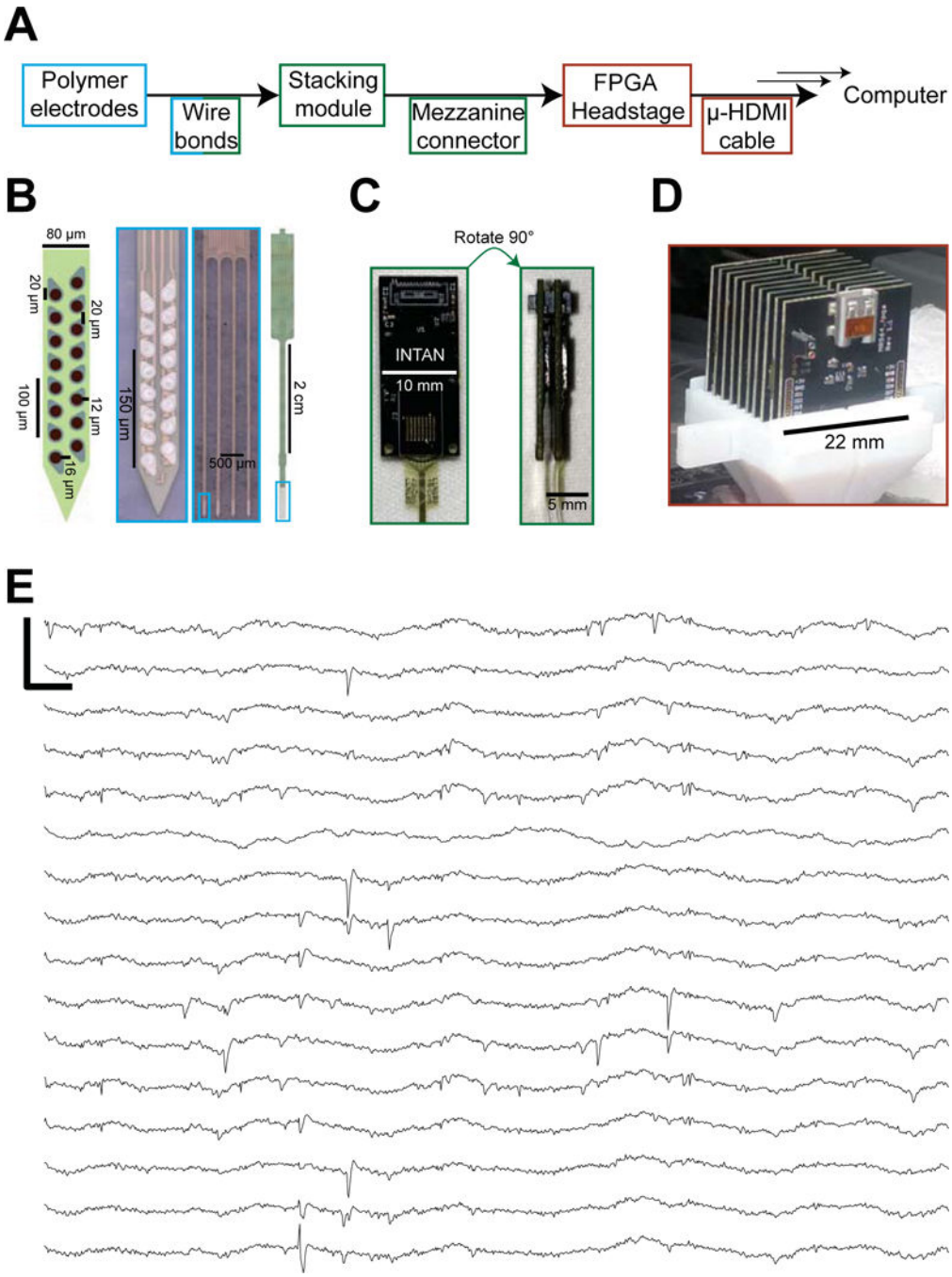

Figure 1. Modular 1024-channel implantation platform overview.

(A) Data path from electrode to computer, with box color corresponding to related components in following subfigures. (B) Polymer electrode array. Left, schematic of 16-channel shank of polymer array designed for single-unit recording. All contacts are circular with 20 μm diameter with 20 μm edge-to-edge spacing. Shank is 14 μm thick. Middle-left, image of 16-ch shank. Middle-right, 4-shank (250 μm edge-to-edge spacing), 64-channel array. Right, full polymer array, bond pads at top of array. (C) Left, view of individual 64-channel module with amplifying, digitizing, and multiplexing chip (Intan Technologies)

wire-bonded onto board, and mezzanine-style connector attached at top of board. Right, two modules stacked together. (D) Full 1024-channel, 16-module, recording system stacked into FPGA headstage (SpikeGadgets LLC) during implantation. (E) Raw 100 ms traces from one 16-ch shank. Scalebar corresponds to 1 mv vertically and 5 ms horizontally. Also see Supplemental Figure 1.

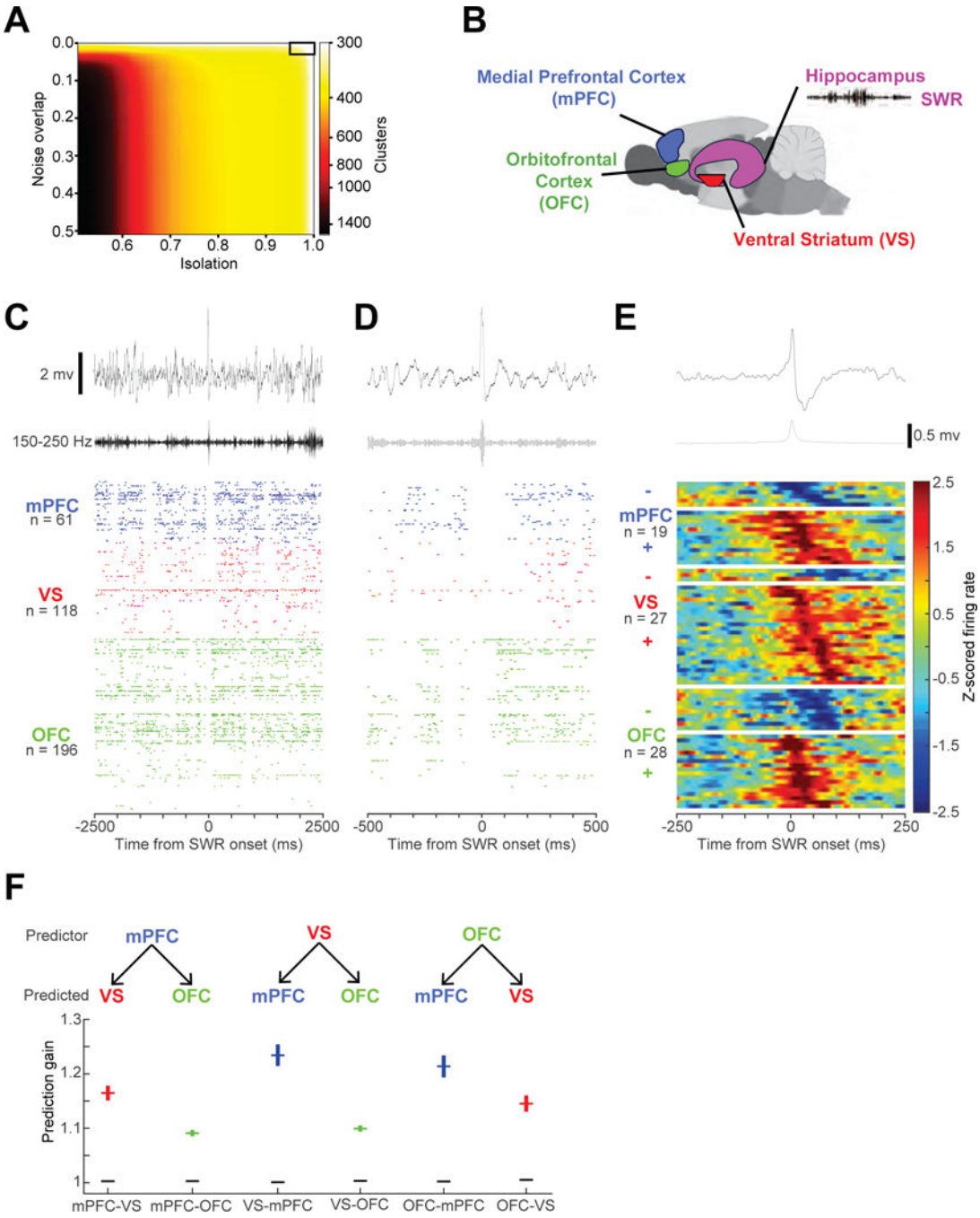

Figure 2. Large-scale, distributed recording.

(A) Number of putative single-unit clusters from 512 channels (of the 1024-channel implant), stratified by quality metric thresholds. Automated curation using MountainSort (noise overlap 0.03, isolation 0.96, black box in upper right) resulted in the identification of 375 single units from the 512 channels. (B) Schematic of the rat brain with targeted regions highlighted. (C) Top, 5 second raw LFP trace from one of 128 channels implanted into Hippocampus, centered on a SWR. Middle, 150 – 250 Hz filtered trace. Bottom, spike rasters from 375 simultaneously recorded neurons from the same time period, with colors

corresponding to the highlighted region. Horizontal axis in ms. (D) As in (C), but for 1 second centered around the same event. (E) Averaged 500 ms traces for average LFP (top), power (middle, 150 – 250 Hz). Bottom, normalized firing rate, peri-SWR histograms for the significantly SWR-modulated neurons, separated by recording location, and ordered by time of trough or time of peak (calculated from 4,046 SWRs). (F) Prediction gain for each set of regions. Top, predictor region, with arrow to predicted region below. Mean prediction gain (horizontal line) ± standard error (vertical lines) for each predictor-predicted set of regions. Color of bar corresponds to each predicted region, as shown in (B). Shuffled prediction gains shown in black. Each of the actual prediction gains was highly significantly greater than the shuffled gains (all p's $< 10^{-10}$; see text for details).

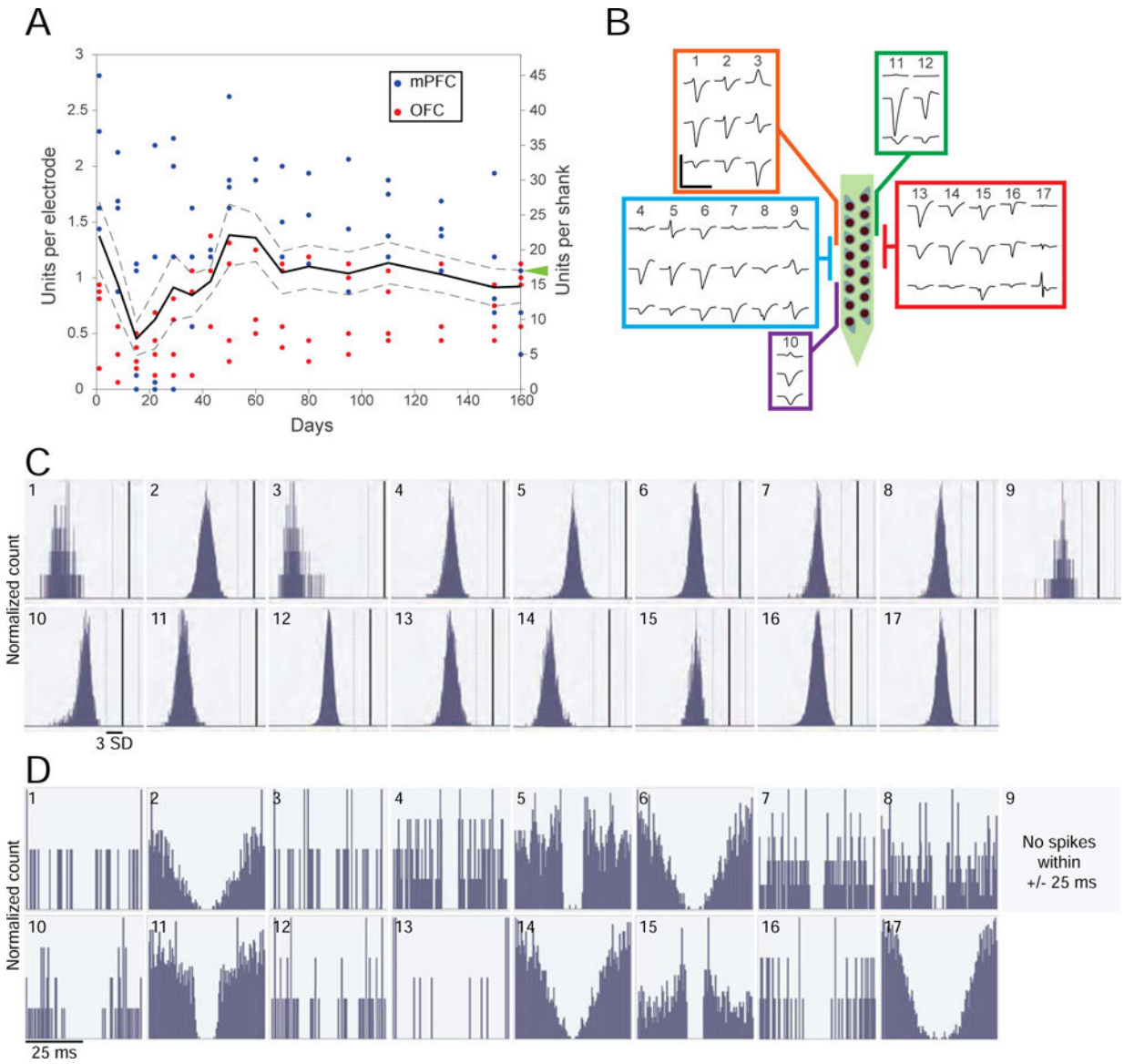

Figure 3. Single-unit recording yield of polymer probes over time.

(A) Single-unit yields for polymer probes per channel (left y-axis) or per 16-ch shank (right y-axis) over 160 days post-implantation (x-axis) in rats. Solid line is the mean cell yield across 8 shanks, dotted lines ± 1 SE. Individual time points per shank are shown as color-coded dots by region. (B) Waveforms and identification number for units clustered for data point with green arrowhead. Scale bar corresponds to 200 μv and 2 ms. Note that the root mean square voltage for the channels on this shank ranged from 15 to 17 μv, and thus all waveforms are substantially larger than the mean activity level. (C) Histograms of event amplitudes for units shown in (B) with unit identification number inset. Vertical black lines designate zero, with the vertical dotted lines representing ± 3 SD, the detection thresholds. Scalebar corresponding to 3 SD and Y-axis normalized for each unit. (D) Spike autocorrelograms for the units shown in (B) and (C), spanning ± 25 ms and bin size of 0.5

ms. Scalebar corresponds to 25 ms and Y-axis is normalized for each unit. Also see Supplemental Figure 2.

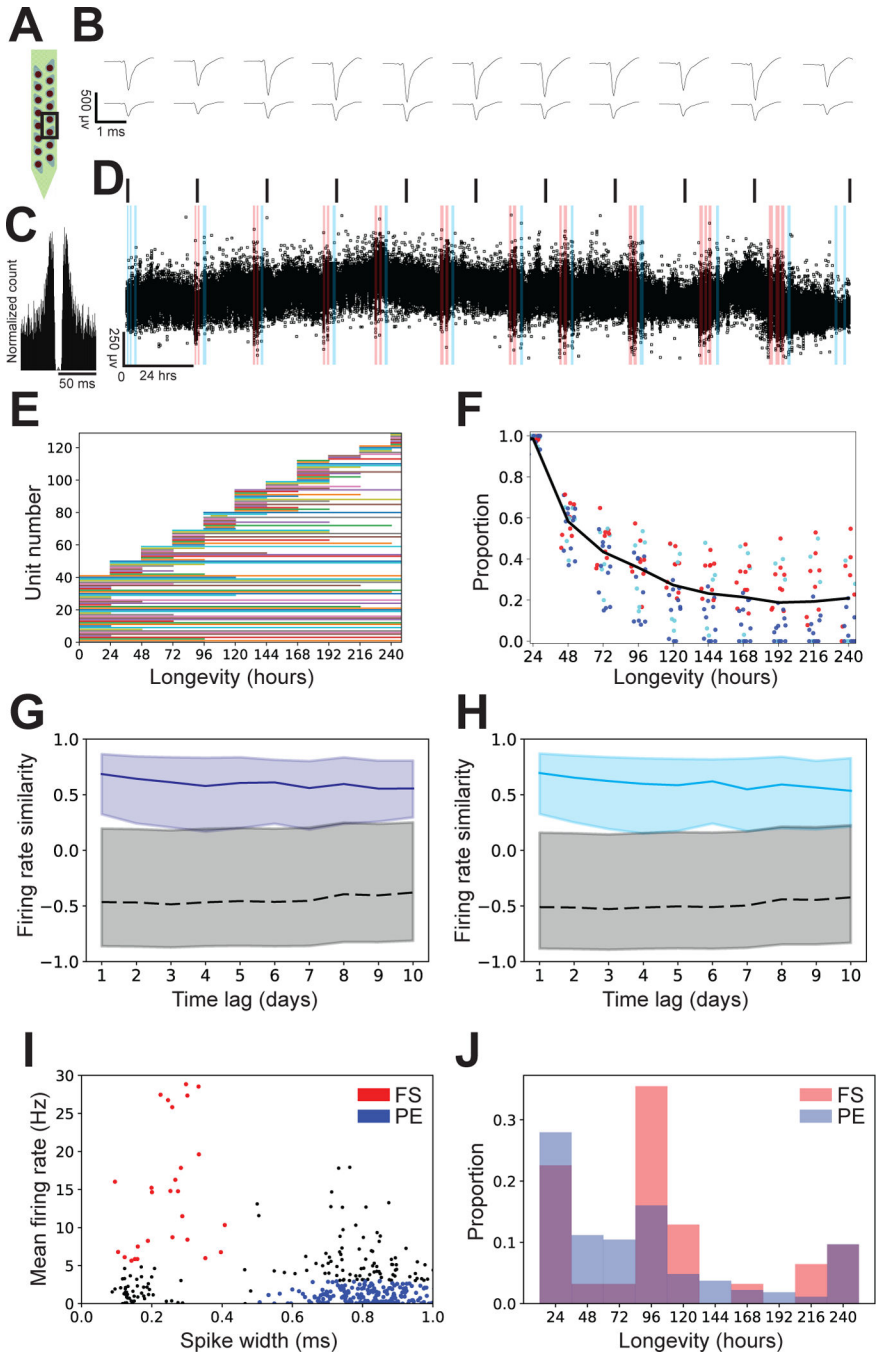

Figure 4. Tracking individual single-units over time.

(A-D) Example unit tracked for 248 hours of continuous recording. (A) Geometric layout of recording channels, with 2 boxed channels on which the unit was detected. (B) Average waveforms (bandpass filtered 300 – 6000 Hz) for the two channels indicated in (A), calculated for 1-hour time bins every 24 hours, except for the last bin, which corresponds to the last hour of recording (hour 247 to 248). Scale bar corresponds to 500 µv and 1 ms. (C) Autocorrelogram for the unit, calculated over all 248 hours. X-axis corresponds to ± 50 ms in 0.5 ms bins, y-axis normalized to largest bin. (D) Spike amplitude (bandpass filtered 300

– 6000 Hz) over length of continuous recording, for all ~700,000 events in the time period. Each event is shown as a black square, allowing all outliers to be seen. Top, black lines correspond to the 1-hour bins from which average waveforms in (B) are calculated. Shading corresponds to spatial behavioral task performance either in room A (blue), or room B (red, see Methods for more details). Non-shaded times correspond to periods when the animal was either in the rest box or its home cage. (E) Period over which each unit could be tracked for one shank. (See Supplemental Fig. 3 for all other shanks). (F) Proportion of units that could be tracked for a given length of time. Black is the total across 26 shanks. Each point corresponds to an individual shank from animal A (blue, 11 shanks), animal B (cyan, 6 shanks), or animal C (red, 9 shanks), jittered in the x-dimension for ease of visualization. (G) Median within-unit firing rate similarity ± 1 quartile (shading between 25th and 75th percentiles) for all 3 animals (dark blue), calculated during behavioral task performance in room one for low velocity times (< 4 cm / s) alongside the median of all between-unit time lagged similarities ± 1 quartile (shading between 25th and 75th percentiles), matched for shank and time-lag (grey). (H) As in (G), but for high velocity times (≥ 4 cm / s). Within-unit firing rate similarity in light blue and between-unit time lagged similarities in grey. (I) Spike width and mean firing rate for all units in the first hour of recording. Fast-spiking (FS) units are shown in red, defined by mean firing rates > 5 Hz and spike widths < 0.5 ms. Putative excitatory (PE) units are shown in blue, defined by mean firing rates < 3 Hz and spike widths > 0.5 ms. All other units are shown in black. (J) Histogram of FS units (red) and PE units (blue) showing number of hours that units could be tracked. Also see Supplemental Figure 3.